

Stability of Néel-type skyrmion lattice against oblique magnetic fields in GaV_4S_8 and GaV_4Se_8

B. Gross,¹ S. Philipp,¹ K. Geirhos,² A. Mehlin,¹ S. Bordács,^{3,4}
V. Tsurkan,^{2,5} A. Leonov,⁶ I. Kézsmárki,² and M. Poggio^{1,7}

¹*Department of Physics, University of Basel, 4056 Basel, Switzerland*

²*Experimental Physics V, Center for Electronic Correlations and Magnetism,
University of Augsburg, 86159 Augsburg, Germany*

³*Department of Physics, Budapest University of Technology and Economics, 1111 Budapest, Hungary*

⁴*Hungarian Academy of Sciences, Premium Postdoctor Program, 1051 Budapest, Hungary*

⁵*Institute of Applied Physics, MD-2028 Chisinau, Republic of Moldova*

⁶*Department of Chemistry, Faculty of Science, Hiroshima University
Kagamiyama, Higashi Hiroshima, Hiroshima 739-8526, Japan*

⁷*Swiss Nanoscience Institute, University of Basel, 4056 Basel, Switzerland*

The orientation of Néel-type skyrmions in the lacunar spinels GaV_4S_8 and GaV_4Se_8 is tied to the polar axes of their underlying crystal structure through the Dzyaloshinskii-Moriya interaction. In these crystals, the skyrmion lattice phase exists for externally applied magnetic fields parallel to these axes and withstands oblique magnetic fields up to some critical angle. Here, we map out the stability of the skyrmion lattice phase in both crystals as a function of field angle and magnitude using dynamic cantilever magnetometry. The measured phase diagrams reproduce the major features predicted by a recent theoretical model, including a reentrant cycloidal phase in GaV_4Se_8 . Nonetheless, we observe a greater robustness of the skyrmion phase to oblique fields, suggesting possible refinements to the model. Besides identifying transitions between the cycloidal, skyrmion lattice, and ferromagnetic states in the bulk, we measure additional anomalies in GaV_4Se_8 and assign them to magnetic states confined to polar structural domain walls.

I. INTRODUCTION

The discovery of the nanometer-scale magnetization configurations known as magnetic skyrmions¹ has spurred renewed interest in non-centrosymmetric magnets. The lack of inversion symmetry in these crystals gives rise to an asymmetric exchange coupling, known as the Dzyaloshinskii-Moriya interaction (DMI), which manifests itself in the continuum approximation of the magnetic order parameter as Lifshitz invariants (LIs) involving first derivatives of the magnetization \mathbf{M} with respect to the spatial coordinates:

$$\mathcal{L}_{i,j}^{(k)} = M_i \frac{\partial M_j}{\partial x_k} - M_j \frac{\partial M_i}{\partial x_k}. \quad (1)$$

Crystal symmetry determines the allowed LIs, i.e. a certain combination of first order derivatives, which – in competition with the spin stiffness – stabilize modulated spin-textures such as spirals and skyrmions and determine their internal structure^{2,3}. Both skyrmion lattices (SkLs)^{4,5} and isolated skyrmions⁶ have now been observed in either bulk or nanostructured noncentrosymmetric crystals. Their topologically protected spin-texture, which is stable even at room temperature⁷, their nanometer-scale size, and their easy manipulation via electric currents and fields^{8–12} make skyrmions a promising platform for information storage and processing applications^{13,14}.

Until recently, most investigations in bulk crystals have focused on Bloch-type skyrmions, in which the local magnetization rotates perpendicular to the radial direction moving from the skyrmion core to the far field. This

type of skyrmion has been observed in chiral cubic helimagnets with B20 structure such as MnSi ¹, FeGe ¹⁵, or Cu_2OSeO_3 ¹⁶. Recently, Néel-type skyrmions, in which the local magnetization rotates in a plane containing the radial direction, have been observed in bulk GaV_4S_8 , GaV_4Se_8 ^{12,17–21}, and GaMo_4S_8 ²². These materials crystallize in the cubic lacunar spinel structure^{23–30}, which becomes polar below ~ 45 K and the point symmetry is reduced from T_d to C_{3v} ^{17,30–32}. Since the magnetic order develops in the polar phase, these compounds are multiferroic. Furthermore, the skyrmions possess a non-trivial electric polarization pattern due to the magnetoelectric effect³⁰, which may enable nearly dissipation free manipulation of the magnetic order by electric fields³¹.

In addition to obvious differences in the spin texture of Bloch- and Néel-type skyrmions, the phase diagrams of cubic helimagnets and polar skyrmion hosts are markedly different. In cubic helimagnets, the LI has an isotropic form $w_{\text{DMI}} = \mathbf{M} \cdot (\nabla \times \mathbf{M})$. Therefore, the plane of the SkL aligns itself to be nearly perpendicular to the applied magnetic field, irrespective of the field's direction. The isotropic LI also results in a narrow stability range of for Bloch-type skyrmions in the vicinity of the magnetic ordering temperature, due to competition with the longitudinal conical phase^{1,15}. In contrast, C_{nv} ($n \geq 3$) symmetry only allows an axially symmetric LI. Therefore, in polar skyrmion hosts, modulated magnetic structures with wave vectors perpendicular to the high symmetry, polar axis are favoured. In these compounds, the orientation of Néel skyrmions is locked to the polar axis rather than the applied magnetic field. Thus, instead of tilting the plane of the SkL, oblique applied fields distort the configuration

of the Néel skyrmions and displace their cores³³. This property has two consequences on the magnetic phase diagram of such materials: 1) the SkL phase is more robust than in cubic helimagnets, because the conical phase is suppressed, and 2) its stability range depends on the direction of the applied field. In addition to the polar LI, the second order magnetic anisotropy allowed in this symmetry can also modify the phase diagram. In the case of GaV₄S₈, strong easy-axis anisotropy³² suppresses the modulated phases at low temperature¹⁹, whereas in GaV₄Se₈ easy-plane anisotropy helps to stabilize the SkL phase down to the lowest temperatures^{12,18,20}.

Here, we use dynamic cantilever magnetometry (DCM)^{34–36} to map the magnetic phase boundaries in GaV₄S₈ and GaV₄Se₈ as a function of the strength and orientation of magnetic field. We determine the corresponding phase diagrams, which reproduce the major features predicted by a recent theoretical model³³. The measurements constitute a direct experimental confirmation of the robustness of Néel-type skyrmions to oblique magnetic fields in two materials with uniaxial magnetic anisotropy of opposite signs. In addition to magnetic transitions between the cycloidal, SkL, and field-polarized ferromagnetic states, in GaV₄Se₈, we also observe sharp anomalies in the torque, which we assign to field-driven transformations of magnetic states confined to polar domain walls (DWs).

II. DYNAMIC CANTILEVER MAGNETOMETRY

In DCM, the sample under investigation is attached to the end of a cantilever, which is driven into self-oscillation at its resonance frequency f . Changes in this resonance frequency $\Delta f = f - f_0$ are measured as a function of the uniform applied magnetic field \mathbf{H} , where f_0 is the resonance frequency at $H = 0$. Δf reveals the curvature of the magnetic energy E_m with respect to rotations about the cantilever oscillation axis^{34,35}:

$$\Delta f = \frac{f_0}{2k_0 l_e^2} \left(\frac{\partial^2 E_m}{\partial \theta_c^2} \Big|_{\theta_c=0} \right), \quad (2)$$

where k_0 is the cantilever's spring constant, l_e its effective length, and θ_c its angle of oscillation. Measurements of this magnetic curvature are particularly useful for identifying magnetic phase transitions³⁴, since – just as the magnetic susceptibility – it should be discontinuous for both first and second order phase transitions³⁷.

DCM measurements are carried out in a vibration-isolated closed-cycle cryostat. The pressure in the sample chamber is less than 10^{-6} mbar and the temperature can be stabilized between 4 and 300 K. Using an external rotatable superconducting magnet, magnetic fields up to 4.5 T can be applied along any direction spanning 120° in the plane of cantilever oscillation, as shown in Fig. 1. $\hat{\mathbf{x}}$ in our coordinate system is defined by the

cantilever's long axis, while $\hat{\mathbf{y}}$ coincides with its axis of oscillation. β is the angle between \mathbf{H} and $\hat{\mathbf{x}}$ in the xz -plane. The cantilever's motion is read out using an optical fiber interferometer using 100 nW of laser light at 1550 nm³⁸. A piezoelectric actuator mechanically drives the cantilever at f with a constant oscillation amplitude of a few tens of nanometers (corresponding to oscillation angles of tens of microradians) using a feedback loop implemented by a field-programmable gate array. This process enables the fast and accurate extraction of f from the cantilever deflection signal as well as providing a measure of the dissipation Γ , which described the system's rate of energy loss: $dE/dt = -\Gamma l_e^2 \dot{\theta}_c^2$. In order to maintain a constant oscillation amplitude, the cantilever must be driven with a force $F = \Gamma l_e \dot{\theta}_c$, such that any losses due to dissipation are compensated. The voltage amplitude used to drive the piezoelectric actuator is therefore proportional to $\Gamma = \Gamma_0 + \Gamma_m$ where Γ_0 is the cantilever's intrinsic mechanical dissipation at $H = 0$ and Γ_m represents magnetic losses. Given that Γ_m reflects the sample's magnetic relaxation, Γ should undergo abrupt changes at magnetic phase transitions. We therefore use both measurements of the magnetic curvature and dissipation, combined with knowledge from other measurements^{12,17–20}, to map the low-temperature magnetic phase diagrams of GaV₄S₈ and GaV₄Se₈ as a function of \mathbf{H} .

III. SAMPLES

Single crystals of GaV₄S₈ and GaV₄Se₈ are grown by a chemical transport reaction method using iodine as a transport agent¹⁷. X-ray diffraction measurements of both sample materials show impurity-free single-crystals³⁰. For the DCM measurement, we attach individual crystals of GaV₄S₈ and GaV₄Se₈, which are a few tens of micrometers in size, to the ends of commercial Si cantilevers (NanosensorsTMTL-cont) using non-magnetic epoxy, as shown in Fig. 1. These cantilevers are 440 μm -long, 50 μm -wide, and 2.3 μm -thick. Unloaded, they have resonance frequencies of about 16 kHz, quality factors around 5×10^5 , and spring constants of 300 mN/m. Due to the additional mass of the samples, the resonance frequency of a loaded cantilever shifts to around 3 kHz.

Both samples are attached near the free end of the cantilever with the (001) surface pressed flat against the Si surface. The orientation of the GaV₄S₈ and GaV₄Se₈ samples differs and can be roughly estimated from optical and scanning electron microscope (SEM) images. The resultant direction of each sample's crystalline axes with respect to the cantilever is shown in Fig. 1: specifically the approximate orientation of the four cubic $\langle 111 \rangle$ axes $\hat{\mathbf{c}}_i$ ($i = 1, 2, 3, 4$) is shown in black, red, green, and blue.

Both GaV₄S₈ and GaV₄Se₈ undergo a Jahn-Teller structural phase transition from a non-centrosymmetric cubic to a rhombohedral structure at 44 K and 42 K, respectively^{11,12,29,30}. The transition is characterized by

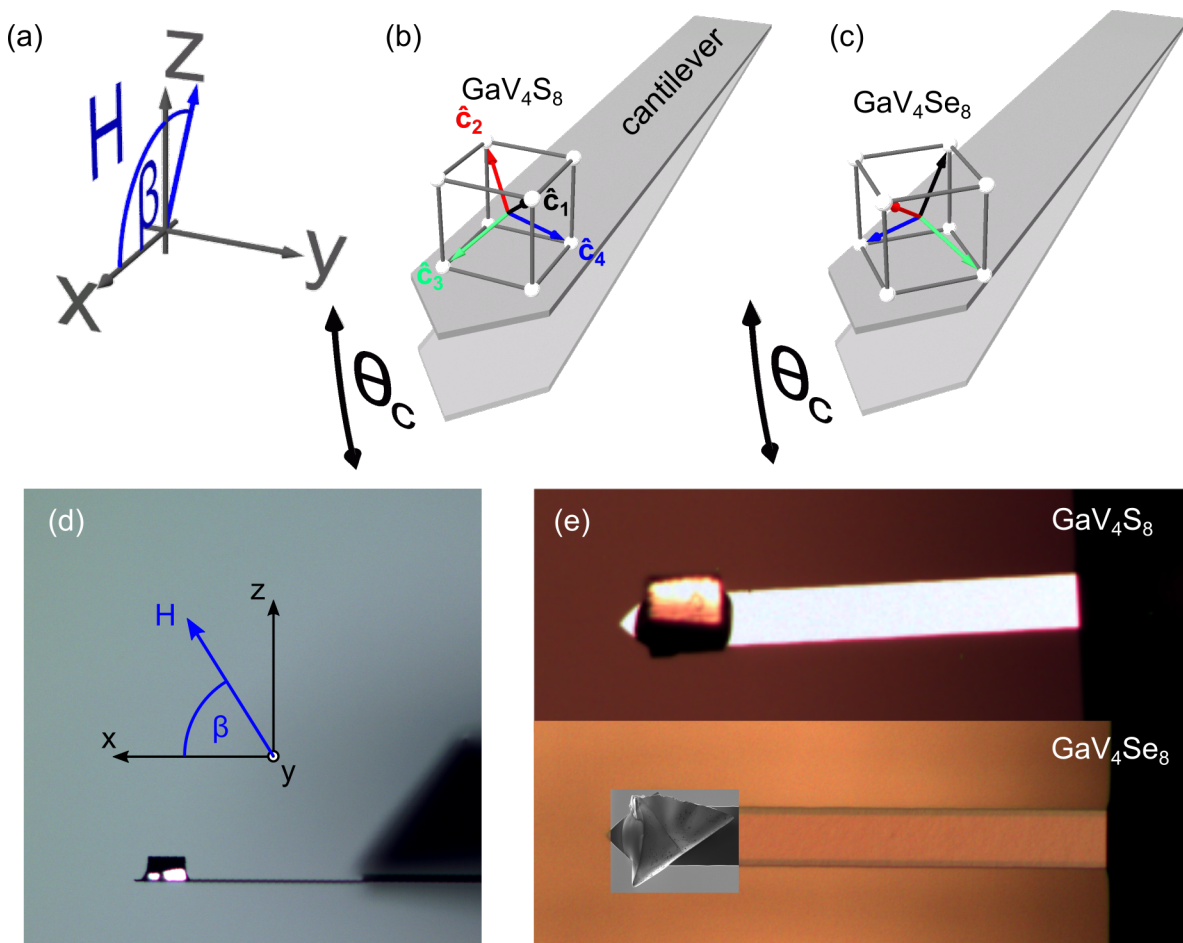


Figure 1. Schematics of the measurement setup. (a) shows the coordinate system and the definition of β as the angle between \mathbf{H} and \hat{x} . (b) and (c) show the cantilever, its oscillation angle θ_c , and the crystalline axes of the measured sample. Black, red, green, and blue lines correspond to the four $\hat{\mathbf{c}}_i$. (d) shows the orientation of \mathbf{H} with respect to an optical image of a sample and cantilever. (e) Composite optical and scanning electron micrographs of the measured GaV_4S_8 and GaV_4Se_8 samples mounted on their respective cantilevers.

a stretching of the cubic unit cell along one of the four cubic body diagonals $\hat{\mathbf{c}}_i$, resulting in four different structural domains. The rhombohedral distortion also gives rise to polarization along $\hat{\mathbf{c}}_i$, making these the polar axes of the system. The multi-domain state is composed of sub-micrometer-thick sheets of these four different rhombohedral polar domains, which we label P_i ^{20,21}. The polar axis $\hat{\mathbf{c}}_i$ also corresponds to the axis of magnetic anisotropy in the respective rhombohedral domain state. In GaV_4S_8 , the uniaxial anisotropy is of easy-axis type, while in GaV_4Se_8 it is of easy-plane type^{17,18,32}. In both materials, measurements indicate the presence of modulated magnetic phases including a cycloidal (Cyc) state, a Néel-type SkL, and a field polarized ferromagnetic (FM) phase^{17,18}. The population of multiple rhombohedral domains at low temperature complicates the determination of the magnetic phase diagram, because for any given orientation of the applied field \mathbf{H} , there can be up to four different angles, α_i , between \mathbf{H} and $\hat{\mathbf{c}}_i$. As a result, for an arbitrary orientation of \mathbf{H} , a single phase transition

can appear at up to four different values of H , depending on the projections of \mathbf{H} on each $\hat{\mathbf{c}}_i$. Although the application of a large electric field upon cooling through the structural phase transition has been shown to polarize GaV_4S_8 and GaV_4Se_8 samples such that only a single domain is populated^{11,12}, it is practically challenging to apply such fields in a DCM apparatus.

IV. MEASUREMENTS

A. GaV_4S_8

Fig. 2 shows DCM measurements of $\Delta f(H)$ and $\Gamma_m(H)$ in GaV_4S_8 for different temperatures T . Data shown in Fig. 2 (a) and (b) are collected with \mathbf{H} aligned along the cantilever's long axis ($\beta = 0$), i.e. approximately $\mathbf{H} \parallel [100]$. In this configuration, the angles α_i between \mathbf{H} and the four $\hat{\mathbf{c}}_i$ are the same within the precision of the sample orientation, i.e. within a few

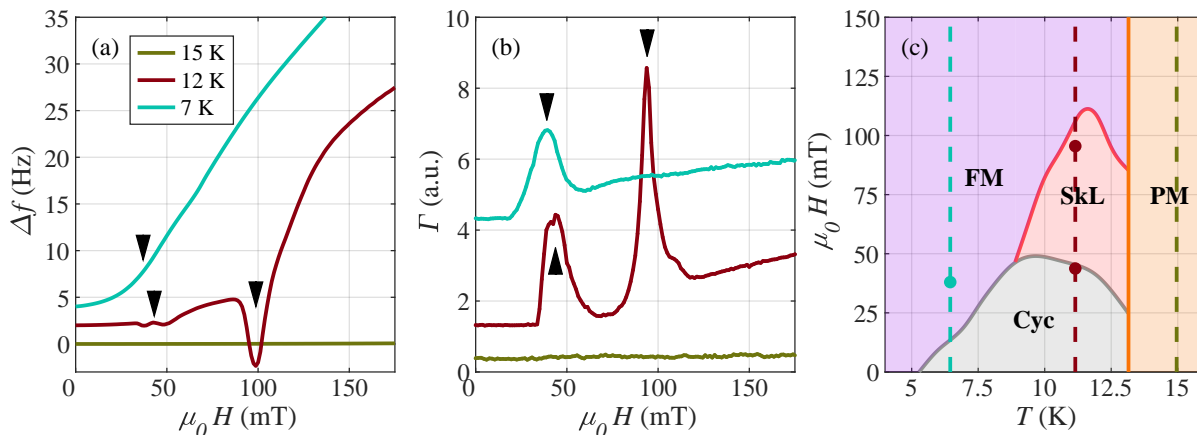


Figure 2. Temperature and field dependence of magnetic phase transitions measured by DCM in GaV_4S_8 . (a) DCM measurements of (a) $\Delta f(H)$ and (b) $\Gamma(H)$ taken at $T = 7, 12,$ and 15 K in cyan, maroon, and brown, respectively. Curves are shifted for better visibility. $\beta = 0$, i.e. approximately $\mathbf{H} \parallel [100]$. Arrows indicate features corresponding to phase transitions. (c) Sketch of the expected magnetic phase diagram as a function of temperature and applied field for $\mathbf{H} \parallel [100]$ ¹⁷. Color-coded dashed lines and points correspond to temperatures and measured features in (a) and (b).

degrees. Consequently, each magnetic phase transition should occur at a similar value of H for each domain. In this particularly simple case, we compare $\Delta f(H)$ and $\Gamma(H)$ at different temperatures to the corresponding magnetic phase diagram measured by Kézsmárki et al.¹⁷ and shown schematically in Fig. 2 (c). Where metamagnetic transitions are expected, they manifest themselves as dips in $\Delta f(H)$ and peaks in $\Gamma_m(H)$. At $T = 12$ K, the two features at 45 and 100 mT (indicated by arrows) correspond to the Cyc-to-SkL and the SkL-to-FM phase transitions, respectively. The double dip (peak) feature in $\Delta f(H)$ ($\Gamma(H)$) comes from the imperfect alignment of the sample's crystalline axes with the coordinate system of our measurement setup, resulting in a difference in α_i for each domain. At $T = 7$ K only one feature is found, corresponding to the Cyc-to-FM transition, while at $T = 15$ K, which is above the magnetic ordering temperature, no features are observed.

\mathbf{H} is rotated approximately in the (010) plane such that, in general, by changing β , we change each α_i differently. As a result, the number of features related to phase transitions and the fields at which they occur can also change. The dependence that we observe is consistent with the orientation of our sample and previous measurements by Kézsmárki et al. In particular, we note that because of the crystal's alignment and its cubic symmetry, the measured curves should repeat themselves upon rotating β by 90° . This periodic behavior can be seen in Fig. 3 (a), where two DCM curves with $\beta = 0$ and 90° nearly overlap; differences, including the splitting of the dips in $\Delta f(H)$ into two dips, are again related to the slight misalignment of the sample's crystalline axes with respect to the applied field, resulting in slightly different α_i for each domain. In the curve taken with $\beta = 40^\circ$ (approximately $\mathbf{H} \parallel [101]$) shown in Fig. 3 (b), we observe four features. The features observed at 35 and 60 mT are

the Cyc-to-SkL and the SkL-to-FM phase transitions, respectively, also observed by Kézsmárki et al. These transitions correspond to the P_4 and P_1 domains (blue and black in Fig. 1) with $\alpha_4 = 31.7^\circ$ and $\alpha_1 = 39.2^\circ$. The two transitions at 320 mT and 370 mT correspond to the Cyc-to-FM transitions in the P_3 and P_2 domains (green and red in Fig. 1), where $\alpha_3 = 84.5^\circ$ and $\alpha_2 = 88.8^\circ$. As before, the mismatches $\alpha_4 \neq \alpha_1$ and $\alpha_3 \neq \alpha_2$ and the resulting pair of split features are due to the crystal's imperfect alignment with the applied field.

Using the measured features in $\Delta f(H)$ and $\Gamma_m(H)$, we map the magnetic phase transitions of GaV_4S_8 as a function of H and β . After initializing the system with a large external field $H = 1$ T, DCM measurements are made by stepping H toward zero at a fixed β and T . The angular dependence over the range $-5^\circ < \beta < 100^\circ$ is recorded at $T = 11$ K by changing β in steps of 2.5° and repeating the measurement. We plot the features identified in these measurements as open circles in Figs 4 (a) and (b). By comparing our data taken for a few magnetic field orientations with the phase diagram reported by Kézsmárki et al.¹⁷, we assign each feature to a certain type of transition (i.e. Cyc-to-FM, Cyc-to-SkL, SkL-to-FM) occurring in a certain domain state (P_1, P_2, P_3, P_4).

Next, we determine the dependence of the phase boundaries on the orientation of the magnetic field with respect to the axis of the uniaxial magnetic anisotropy. The measured signatures shown as open circles in Figs. 4 (a) and (b) can be fit by assuming that each of the four rhombohedral domains of GaV_4S_8 obeys the magnetic phase diagram shown in (d), plotted as a function of H_{\parallel} and H_{\perp} , the components of \mathbf{H} parallel and perpendicular to the rhombohedral axis $\hat{\mathbf{c}}_i$, respectively. A feature in Δf and Γ observed at certain H and β corresponds to a transition of a particular domain P_i for

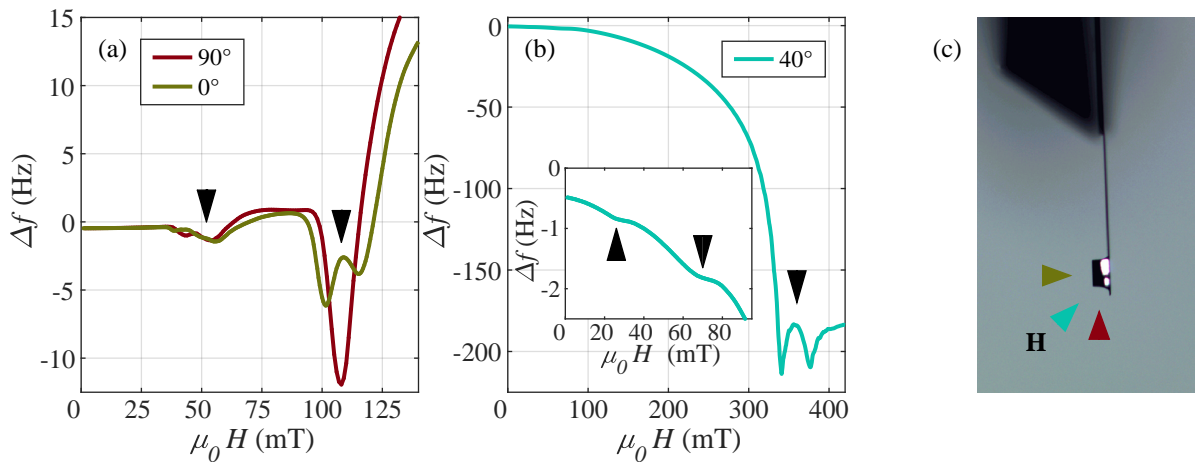


Figure 3. Angular dependence of magnetic phase transitions measured by DCM in GaV_4S_8 . (a), (b) $\Delta f(H)$ at $T = 11$ K for at $\beta = 0, 40$, and 90° in maroon, cyan, and brown, respectively. Arrows indicate features corresponding to phase transitions. Inset: zoomed view of the low-field region. (c) Schematic diagram showing the three measured orientations relative to the sample-loaded cantilever.

a field of magnitude H and angle α_i with respect to $\hat{\mathbf{c}}_i$, as shown in Fig. 4 (c). The magnitude H and the angle α_i at which each feature occurs, correspond to a point on a phase boundary in the diagram of Fig. 4 (d), through $H_{\parallel} = H \cos \alpha_i$ and $H_{\perp} = H \sin \alpha_i$. This phase diagram reflects the general form suggested by Leonov and Kézsmárki³³. Phase boundaries corresponding to the diagram are also plotted as a function of β and H in Figs. 4 (a) and (b) to show their agreement with the measurements. They appear as solid lines, which are color-coded according to the domain to which they belong. An Euler rotation of the crystal ($-5.0, 0.2$ and 10.0°) with respect to ideal configuration, shown in Fig. 1 (b), is required such that the phase boundaries corresponding to the different domain states collapse onto the single boundary diagram of Fig. 4 (d).

The agreement between the measured features and fit phase boundaries allows us to eliminate complications arising from the multi-domain nature of the crystal and, thus, to extract a the general magnetic phase diagram of GaV_4S_8 as function of field applied parallel and perpendicular to the anisotropy axis. The position of the intersection between the different phase transitions in Fig. 4 (d) shows that the SkL phase in GaV_4S_8 persists in oblique fields up to a threshold angle as large as $\alpha_{\max} = 77^\circ$. For larger α , the cycloidal state directly transforms to the ferromagnetic state upon increasing H . The extent of the SkL phase shows stronger stability against fields applied perpendicular to the anisotropy axis (up to $H_{\perp} = 200$ mT) than fields applied parallel (up to $H_{\parallel} = 65$ mT). This critical angle α_{\max} is larger than predicted by Leonov and Kézsmárki³³.

B. GaV_4Se_8

We apply the same experimental procedure to explore the magnetic phase diagram of GaV_4Se_8 . In this case, \mathbf{H} is rotated approximately in the $(1\bar{1}0)$ plane. Figs. 5 (a) and (b) show the angular dependence of the features, as extracted from measurements of $\Delta f(H)$ and $\Gamma_m(H)$ at $T = 12$ K. Using previous measurements made by Bordács et al. along particular crystalline directions¹⁸, as well as neutron diffraction data by Geirhos et al.²⁰ for guidance, we assign each feature to a transition between Cyc, SkL, or FM states for a certain domain and color-code it accordingly.

Once again, the measured features are shown as open circles in Figs. 5 (a) and (b) and can be fit by assuming that each of the four rhombohedral domains obeys a single magnetic phase diagram shown in (d). The magnitude of the applied field H and its angle α_i with respect to the assigned domain's rhombohedral axis $\hat{\mathbf{c}}_i$ put each feature on one of the phase boundaries depicted in Fig. 5 (d). Phase boundaries corresponding to the phase diagram are plotted in Figs. 5 (a) and (b) for comparison with the measured data. They appear as solid lines, which are color-coded according to the domain. Similarly to GaV_4S_8 , the overall form of the phase diagram agrees with that suggested by Leonov and Kézsmárki³³, although there are minor quantitative differences between our results and the theoretical predictions. Note that the rotation plane of \mathbf{H} , approximately $(1\bar{1}0)$, contains $\hat{\mathbf{c}}_1$ and $\hat{\mathbf{c}}_2$, but not $\hat{\mathbf{c}}_3$ and $\hat{\mathbf{c}}_4$. An Euler rotation of the crystal ($-14, -1$ and 7°) with respect to ideal configuration, shown in Fig. 1 (c), is required such that the phase boundaries corresponding to the different domain states (P_1, P_2, P_3, P_4) collapse onto the single boundary diagram of Fig. 5 (d). We find additional anomalies in both $\Delta f(H)$ and $\Gamma_m(H)$, that cannot be ascribed to the

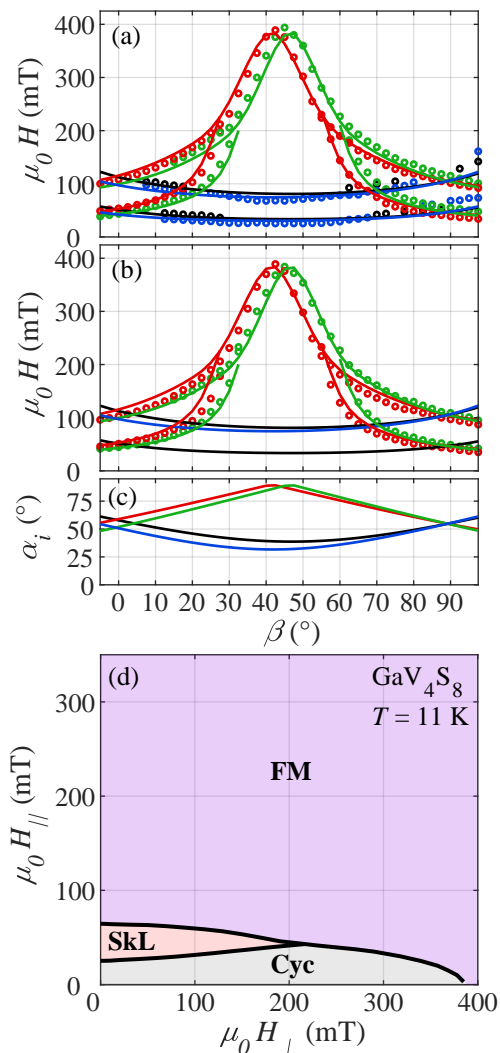


Figure 4. Magnetic phase transitions measured in GaV_4S_8 at $T = 11$ K. Features extracted from DCM measurement of (a) $\Delta f(H)$ and (b) $\Gamma(H)$ are plotted as open circles as a function of β . Black, red, green, and blue circles correspond to domains P_1 , P_2 , P_3 , and P_4 , respectively. Color-coded lines indicate phase boundaries for each domain according to the phase diagram in (d). (c) Angle α_i between the corresponding \hat{c}_i and the external field \mathbf{H} vs. β for all four rhombohedral domains, using the same color code as in (a) and (b). (d) Best-fit magnetic phase diagram for single-domain GaV_4S_8 as a function of field applied perpendicular and parallel to the axis of symmetry.

boundaries between the Cyc, SkL, and FM phases. We suspect that these anomalies originate from the formation of magnetic textures localized at structural DWs, as discussed in section IV C.

For the black and red domains, which are the only two experiencing sufficient H_{\parallel} to reach the SkL phase, the boundaries of the SkL state appear as prominent rain-drop-like shapes in Figs 5 (a) and (b). From the intersection of the SkL with the Cyc phase boundary

in (d), we extract a threshold angle $\alpha_{\max} = 31^\circ$ for the SkL phase in GaV_4Se_8 at $T = 12$ K. Contrary to GaV_4S_8 , the extent of the SkL phase shows stronger stability against fields applied parallel to the anisotropy axis (up to $H_{\parallel} = 340$ mT) than fields applied perpendicular (up to $H_{\perp} = 75$ mT). Furthermore, we note the presence of a reentrant Cyc phase for angles $19^\circ < \alpha_i < 30^\circ$, as predicted by Leonov and Kézsmárki³³. For this range of α_i , two successive first-order phase transitions from Cyc to SkL and back occur as a function of increasing field. The signature of this behavior in DCM is shown in Fig. 5 (e).

C. Magnetic States Confined to Domain Walls in GaV_4Se_8

Geirhos et al. observed anomalies in various macroscopic thermodynamic properties of GaV_4Se_8 , emerging exclusively in crystals with polar multi-domain structure. They suggest a possible scenario for the formation of magnetic states at the structural DWs of the lacunar spinel GaV_4Se_8 ²⁰. Magnetic interactions change step-wise at the DWs and spin textures with different spiral planes, hosted by neighboring domains, need to be matched there. This can, for example, lead to conical magnetic states at the DWs with a different closing field magnitude than bulk magnetic states. Here, we adopt and modify this model in order to analyze its applicability to anomalies observed in our DCM measurements of GaV_4Se_8 , which cannot be assigned to bulk magnetic phase transitions.

In the rhombohedral phase of the studied lacunar spinels, mechanically compatible and charge neutral DWs are normal to $\hat{c}_i + \hat{c}_j$, the sum of the two polar directions of the domain states P_i and P_j separated by the DW, as shown in Fig. 6^{20,21,39}. For example, mechanically and electrically compatible DWs connecting a P_1 (black) and a P_2 (red) domain are parallel to (001) planes, cf. Fig. 6. The same is true for DWs between P_3 (green) and P_4 (blue) domains.

For an arbitrary orientation of the external magnetic field, magnetic states confined to DWs with different orientations are expected to undergo field-induced transitions, similarly to the bulk (in-domain) magnetic states. However, in this case the situation is more complex: The stability of the magnetic states confined to DWs is determined by the orientation of the field with respect to the magnetic anisotropy axes of adjacent domains and to the DW itself.

It is reasonable to assume, that the angle, γ_n , between \mathbf{H} and the normal of the DW planes, given by $\hat{c}_i + \hat{c}_j$, plays a decisive role in setting the angular range, across which confined states are stable. This leads to three pairs of DWs, as shown in Fig. 6, each sharing the same γ_n for a given \mathbf{H} . For DWs in a pair, however, the relative orientation between the magnetic anisotropy axes of the two domains involved and \mathbf{H} is not the same. For ex-

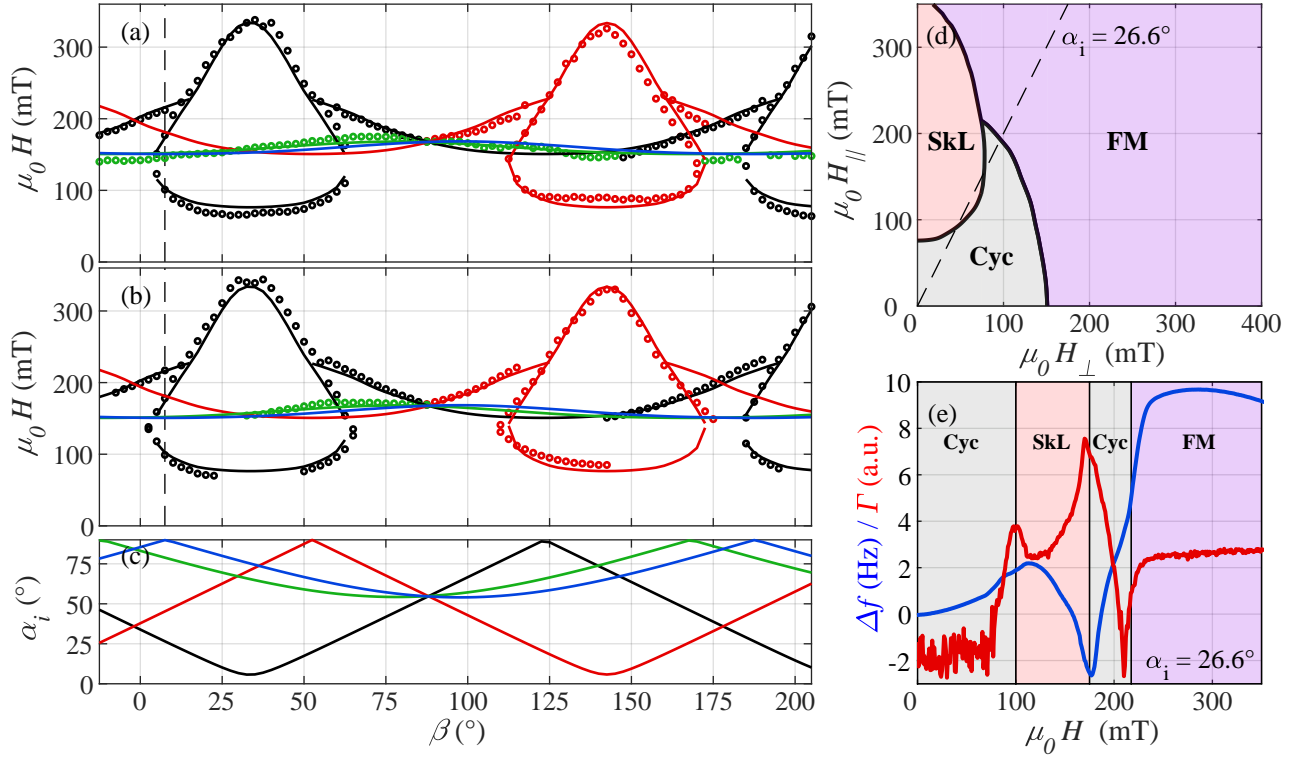


Figure 5. Magnetic phase transitions measured in GaV_4Se_8 at $T = 12$ K. Transitions extracted from DCM measurement of (a) $\Delta f(H)$ and (b) $\Gamma(H)$ are plotted as open circles as a function of β . Black, red, green, and blue circles correspond to transitions for domain P_1 , P_2 , P_3 , and P_4 , respectively. Color-coded lines correspond to phase boundaries for the each color-coded domain as indicated by lines in the phase diagram (d). (c) Angle α_i between corresponding polar axis and the external field \mathbf{H} vs β for all four rhombohedral domains, using the same color code as in (a) and (b). (d) Best-fit magnetic phase diagram for single-domain GaV_4Se_8 as a function of field applied perpendicular and parallel to the axis of symmetry. (e) DCM measurement of $\Delta f(H)$ for $\alpha_i = 26.6^\circ$ ($\beta = 7.5^\circ$) showing the reentrant Cyc phase. These measurements corresponds to line-cuts along the dashed vertical lines in (a) and (b) and the dashed diagonal line in (d).

ample, consider the P_1P_2/P_3P_4 pair: the rotation plane of \mathbf{H} ($1\bar{1}0$) contains the anisotropy axes of P_1 and P_2 , but not the anisotropy axes of P_3 and P_4 ; they span 54° with this plane. We therefore introduce another angle, γ_p , between \mathbf{H} and the difference of the two polar vectors $\hat{\mathbf{c}}_i - \hat{\mathbf{c}}_j$, which lies in the DW plane. Both these angles $\gamma_n(\beta)$ and $\gamma_p(\beta)$, plotted in Fig. 7 (a) and (b), respectively, are expected to affect the stability of the DW-confined magnetic states.

In the angular dependent torque measurements, shown in Figs. 7 (c)-(f), we observe at most four anomalies (open circles) for a given field orientation. Since there are six types of DWs, distinguished by γ_n and γ_p , some transitions, which occur simultaneously in different types of DWs appear as a single anomaly, while some transitions appear not to be experimentally observable. In the following analysis, we take into account an additional anomaly (crosses) between $\beta \simeq 40$ and 130° at field values around 100 mT, which is not present in our DCM measurements, but has been observed in magnetoelectric measurements²⁰.

As a first scenario, we suggest the following assignment of the observed anomalies, shown in Fig. 7 (c).

The anomalies are labeled A to F with an additional index 1 or 2, indicating if they appear for $\beta < 90^\circ$ or $\beta > 90^\circ$, respectively. A_1 and B_1 anomalies are assigned to P_2P_4 DWs; A_2 and B_2 anomalies to P_1P_3 DWs; C_1 and E_1 anomalies to P_2P_3 DWs; the C_2 anomaly to P_1P_4 DWs; D_1 and D_2 anomalies to P_1P_2 DWs; and F_1 and F_2 anomalies to P_3P_4 DWs. In this scenario, all observed anomalies are assigned to transitions of magnetic states confined to DWs, as shown in Fig. 7 (c). In all cases, both domains adjacent to the DWs host the Cyc state and the DW-confined state emerges due to the matching of these two cycloidal patterns. As shown in Fig. 7 (c), no anomaly is observed in angular ranges, where the adjacent domains host magnetic states other than the Cyc. This is true for all the transitions meeting at $\beta \approx 90^\circ$. For example, the B_1 anomaly, which is assigned to transitions on P_2P_4 DWs, would progress above 150 mT for $\beta > 90^\circ$, but because in-domain states within the P_4 domain (blue axis) transform from the Cyc to the FM state for $\beta > 90^\circ$ and $H > 150$ mT, the B_1 anomaly disappears for larger angles. Similarly, the D_1 and D_2 anomalies assigned to transitions in the P_1P_2 DWs are limited by the two skyrmion pockets of the P_1 and P_2

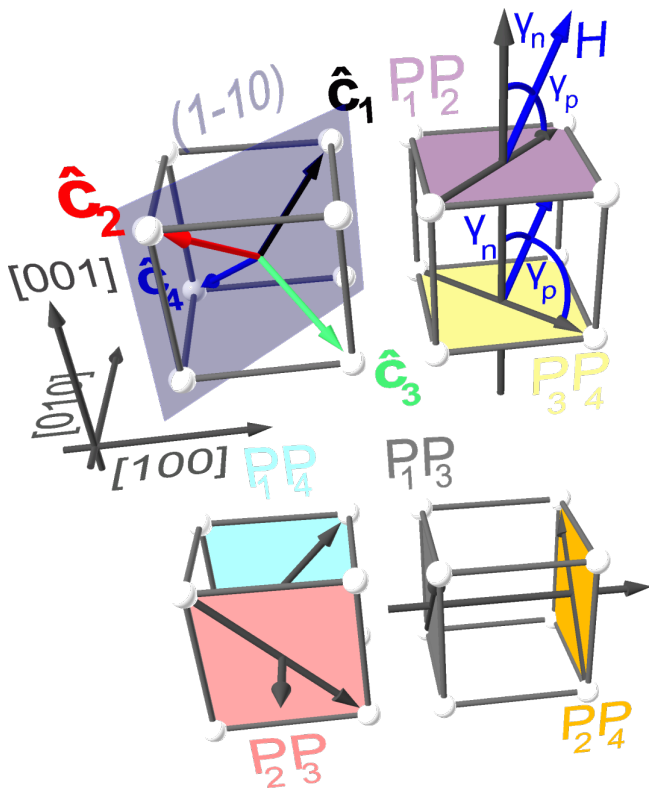


Figure 6. Schematic for understanding the orientation of the 6 different domain walls types. Top left: Directions of the four possible polar axes, P_1 - P_4 , which are the axes of magnetic anisotropy within the corresponding domains. The transparent blue plane indicates the approximate plane of rotation of the external magnetic field. Top right: Mechanically compatible and charge neutral DWs separating P_1 and P_2 domains are parallel to the (001) plane, just as DWs between P_3 and P_4 domains. The former and latter DWs are referred to as P_1P_2 and P_3P_4 , respectively. γ_n (γ_p), the angle between \mathbf{H} and $\hat{\mathbf{c}}_i + \hat{\mathbf{c}}_j$ ($\hat{\mathbf{c}}_i - \hat{\mathbf{c}}_j$), is shown for both DW pairs. Bottom: The other two pairs of DWs sharing the same orientation. The normal vector of the corresponding planes and their labels are indicated for the three cases, as well as the difference vector $\hat{\mathbf{c}}_i - \hat{\mathbf{c}}_j$, unique to each DW type.

domains. The A_1 and A_2 anomalies assigned to P_2P_4 and P_1P_3 , respectively, also do not extend above 150 mT were P_3 and P_4 domains transform from the Cyc to the FM state.

An alternative scenario is an extension of the one suggested by Geirhos et al.²⁰, shown in Fig. 7 (d). Here, B_1 and B_2 anomalies are assigned to transitions at P_3P_4 DWs; A_1 , A_2 , C_1 and C_2 anomalies to transitions at P_1P_2 DWs; D_2 , E_1 , and F_1 anomalies to transitions at P_2P_3 as well as P_2P_4 DWs; and D_1 and F_2 anomalies to transitions at P_1P_3 as well as P_1P_4 DWs. This scenario allows some DW transitions to persist even when one of the adjacent domains leaves the Cyc phase. Such a situation occurs for the P_1P_2 DW transition, which penetrates both the P_1 and the P_2 SkL pockets.

In both scenarios, the mirror symmetry expected

across $\beta \simeq 90^\circ$, as dictated by $\gamma_n(\beta)$ and $\gamma_p(\beta)$ is fulfilled: the transition lines are either symmetric to this point or they have a symmetry-related counterpart. The basis for both scenarios is the occurrence of a distinct magnetic state confined to DWs, and its transition to the FM state at certain critical field, observed as an additional anomaly in the DCM measurement.

The angle of the applied field with the DW-normal, γ_n , and the orientation of its component in the DW-plane, γ_p , appear to be an important parameters in determining the critical field of the DW states.

V. CONCLUSION

We extract the magnetic phase diagrams as a function applied field magnitude and direction for both GaV_4S_8 and GaV_4Se_8 that are in good qualitative agreement with the theoretical predictions of Leonov and Kézsmárki³³, confirming the general validity of their model. This agreement, in turn, provides indirect confirmation that, under oblique applied magnetic field, the axes of Néel-type skyrmions stay locked to the anisotropy axis while their structure distorts and their core displaces. The measurements reproduce the overall structure of the phase diagrams, imposing a maximum angle α_{\max} of magnetic field applied with respect to the anisotropy axis, for which a SkL phase persists. In addition, they show that easy-axis anisotropy – as found in GaV_4S_8 – enhances the robustness of Néel-skyrmions against magnetic fields applied perpendicular to the symmetry axis, while easy-plane anisotropy – as found in GaV_4Se_8 – increases their stability for fields parallel to this axis. Our results also confirm the existence of a reentrant Cyc phase in GaV_4Se_8 , which was anticipated to occur for certain values of easy-plane anisotropy. Finally, anomalies in $\Delta f(H)$ and $\Gamma_m(H)$, which cannot be explained as bulk domain transitions, are consistent with distinct magnetic states confined to polar structural DWs and their transition from the Cyc to FM state, as proposed by Geirhos et al.²⁰.

Nevertheless, the measured magnetic phase diagrams are not in strict quantitative agreement with the predicted ones. For both GaV_4S_8 and GaV_4Se_8 , we are unable to tune the uniaxial anisotropy of the model to match the measured values of threshold angle of the SkL phase $\alpha_{\max} = 77^\circ$ for GaV_4S_8 at $T = 11$ K and 31° for GaV_4Se_8 at $T = 12$ K. This discrepancy suggests that approximations made in the model ignore important details, thus preventing it from capturing the full behavior of the system. Possible improvements to the model include consideration of the anisotropic exchange interaction or extension the model from two to three dimensions. Also, further experimental investigation – especially real-space imaging – of anomalies assigned to transitions of DW-confined magnetic states is required to characterize the spin pattern associated with these states.

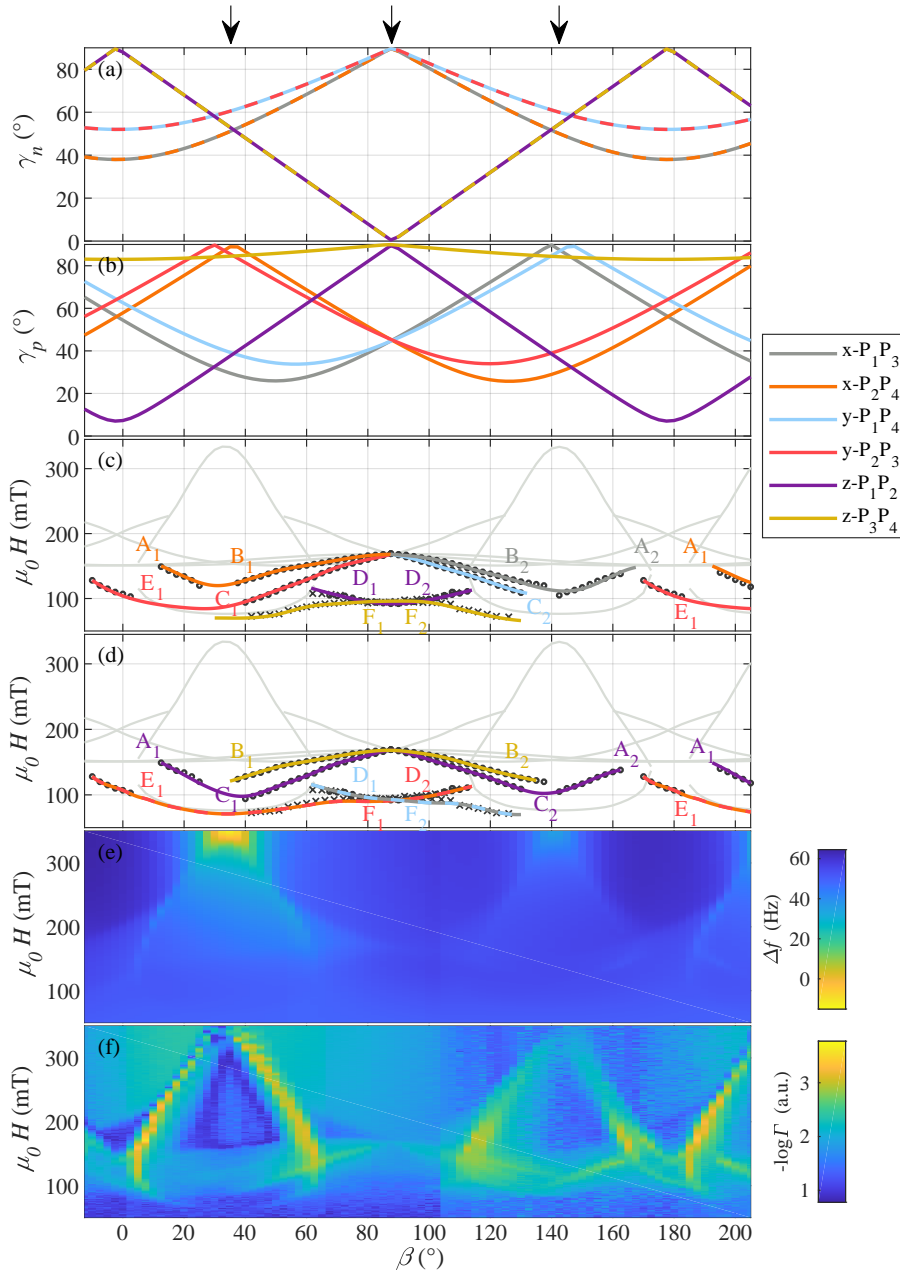


Figure 7. Anomalies in $\Delta f(H)$ and $\Gamma(H)$ assigned to transitions of DW rather than bulk magnetic states. Arrows at the top indicate from left to right the approximate angle β corresponding to the [111], [001] and [11 - 1] directions, respectively. (a) Angle γ_n between the normal vector of a DW and \mathbf{H} plotted against β . The color of the dashed lines shows their correspondence to a DW type in the legend. (b) Angle γ_p between the vector formed by the sum of the polar axis vectors of the two adjacent domains of a DW and \mathbf{H} plotted against β . (c) Transitions extracted from both Δf and Γ that are not assigned to a domain transition (dark gray circles). Crosses show transitions extracted from magnetoelectric measurements²⁰, scaled by about 0.9 to match the DCM data. Colored lines show the suggested assignment of the transitions to DW types as denoted in the legend. (d) Same data as in (c) with a different assignment of transitions. Color map of (e) $\Delta f(H, \beta)$ and (f) $-\log_{10} \Gamma_m(H, \beta)$.

ACKNOWLEDGMENTS

We thank Sascha Martin and his team in the machine shop of the Physics Department at the University of Basel for help building the measurement system. We acknowledge the support of the Canton Aargau and the

Swiss National Science Foundation under Project Grant 200020-159893, via the Sinergia Grant ‘Nanoskyrmionics’ (Grant No. CRSII5-171003), and via the NCCR ‘Quantum Science and Technology (QSIT)’. We further acknowledge the support of the BME-Nanonotechnology and Materials Science FIKP grant of EMMI (Grant

No. BME FIKP-NAT), the Hungarian National Research, Development, and Innovation Office-NKFIH via Grant No. ANN 122879. This research was partly funded by Deutsche Forschungsgemeinschaft (DFG) via

the Transregional Collaborative Research Center TRR 80 “From Electronic correlations to functionality” (Augsburg, Munich, Stuttgart) and by the project ANCD 20.80009.5007.19 (Moldova).

-
- ¹ S. Mühlbauer, B. Binz, F. Jonietz, C. Pfleiderer, A. Rosch, A. Neubauer, R. Georgii, and P. Böni, *Science* **323**, 915 (2009).
- ² A. N. Bogdanov and D. A. Yablonskii, *Zh. Eksp. Teor. Fiz.* **95**, 178 (1989).
- ³ A. Bogdanov and A. Hubert, *J. Magn. Magn. Mater.* **138**, 255 (1994).
- ⁴ X. Z. Yu, Y. Onose, N. Kanazawa, J. H. Park, J. H. Han, Y. Matsui, N. Nagaosa, and Y. Tokura, *Nature* **465**, 901 (2010).
- ⁵ X. Z. Yu, N. Kanazawa, Y. Onose, K. Kimoto, W. Z. Zhang, S. Ishiwata, Y. Matsui, and Y. Tokura, *Nat. Mater.* **10**, 106 (2011).
- ⁶ H. Du, R. Che, L. Kong, X. Zhao, C. Jin, C. Wang, J. Yang, W. Ning, R. Li, C. Jin, X. Chen, J. Zang, Y. Zhang, and M. Tian, *Nat. Commun.* **6**, 8504 (2015).
- ⁷ Y. Tokunaga, X. Z. Yu, J. S. White, H. M. Rønnow, D. Morikawa, Y. Taguchi, and Y. Tokura, *Nat. Commun.* **6**, 7638 (2015).
- ⁸ T. Schulz, R. Ritz, A. Bauer, M. Halder, M. Wagner, C. Franz, C. Pfleiderer, K. Everschor, M. Garst, and A. Rosch, *Nat. Phys.* **8**, 301 (2012).
- ⁹ F. Jonietz, S. Mühlbauer, C. Pfleiderer, A. Neubauer, W. Münzer, A. Bauer, T. Adams, R. Georgii, P. Böni, R. A. Duine, K. Everschor, M. Garst, and A. Rosch, *Science* **330**, 1648 (2010).
- ¹⁰ P.-J. Hsu, A. Kubetzka, A. Finco, N. Romming, K. v. Bergmann, and R. Wiesendanger, *Nat. Nanotechnol.* **12**, 123 (2017).
- ¹¹ E. Ruff, A. Butykai, K. Geirhos, S. Widmann, V. Tsurkan, E. Stefanet, I. Kézsmárki, A. Loidl, and P. Lunkenheimer, *Phys. Rev. B* **96**, 165119 (2017).
- ¹² Y. Fujima, N. Abe, Y. Tokunaga, and T. Arima, *Phys. Rev. B* **95**, 180410 (2017).
- ¹³ J. Sampaio, V. Cros, S. Rohart, A. Thiaville, and A. Fert, *Nat. Nanotechnol.* **8**, 839 (2013).
- ¹⁴ R. Tomasello, E. Martinez, R. Zivieri, L. Torres, M. Carpentieri, and G. Finocchio, *Sci. Rep.* **4**, 6784 (2014).
- ¹⁵ H. Wilhelm, M. Baenitz, M. Schmidt, U. K. Rößler, A. A. Leonov, and A. N. Bogdanov, *Phys. Rev. Lett.* **107**, 127203 (2011).
- ¹⁶ S. Seki, X. Z. Yu, S. Ishiwata, and Y. Tokura, *Science* **336**, 198 (2012).
- ¹⁷ I. Kézsmárki, S. Bordács, P. Milde, E. Neuber, L. M. Eng, J. S. White, H. M. Rønnow, C. D. Dewhurst, M. Mochizuki, K. Yanai, H. Nakamura, D. Ehlers, V. Tsurkan, and A. Loidl, *Nat. Mater.* **14**, 1116 (2015).
- ¹⁸ S. Bordács, A. Butykai, B. G. Szigeti, J. S. White, R. Cubitt, A. O. Leonov, S. Widmann, D. Ehlers, H.-A. K. Nidda, V. Tsurkan, A. Loidl, and I. Kézsmárki, *Sci. Rep.* **7**, 7584 (2017).
- ¹⁹ J. S. White, Á. Butykai, R. Cubitt, D. Honecker, C. D. Dewhurst, L. F. Kiss, V. Tsurkan, and S. Bordács, *Phys. Rev. B* **97**, 020401 (2018).
- ²⁰ K. Geirhos, B. Gross, B. G. Szigeti, A. Mehlin, S. Philipp, J. S. White, R. Cubitt, S. Widmann, S. Ghara, P. Lunkenheimer, V. Tsurkan, A. O. Leonov, S. Bordács, M. Poggio, and I. Kézsmárki, *npj Quantum Mater.*, in press (2020).
- ²¹ A. Butykai, S. Bordács, I. Kézsmárki, V. Tsurkan, A. Loidl, J. Döring, E. Neuber, P. Milde, S. C. Kehr, and L. M. Eng, *Sci. Rep.* **7**, 1 (2017).
- ²² A. Butykai, D. Szaller, L. F. Kiss, L. Balogh, M. Garst, L. DeBeer-Schmitt, T. Waki, Y. Tabata, H. Nakamura, I. Kézsmárki, and S. Bordács, [arXiv:1910.11523](https://arxiv.org/abs/1910.11523) (2019).
- ²³ V. Ta Phuoc, C. Vaju, B. Corraze, R. Sopracase, A. Perucchi, C. Marini, P. Postorino, M. Chlguui, S. Lupi, E. Janod, and L. Cario, *Phys. Rev. Lett.* **110**, 037401 (2013).
- ²⁴ M. M. Abd-Elmeguid, B. Ni, D. I. Khomskii, R. Pocha, D. Johrendt, X. Wang, and K. Syassen, *Phys. Rev. Lett.* **93**, 126403 (2004).
- ²⁵ E. Dorolti, L. Cario, B. Corraze, E. Janod, C. Vaju, H.-J. Koo, E. Kan, and M.-H. Whangbo, *J. Am. Chem. Soc.* **132**, 5704 (2010).
- ²⁶ H.-S. Kim, J. Im, M. J. Han, and H. Jin, *Nat. Commun.* **5**, 3988 (2014).
- ²⁷ V. Guiot, L. Cario, E. Janod, B. Corraze, V. T. Phuoc, M. Rozenberg, P. Stoliar, T. Cren, and D. Roditchev, *Nat. Commun.* **4**, 1722 (2013).
- ²⁸ K. Singh, C. Simon, E. Cannuccia, M.-B. Lepetit, B. Corraze, E. Janod, and L. Cario, *Phys. Rev. Lett.* **113**, 137602 (2014).
- ²⁹ R. Pocha, D. Johrendt, and R. Pöttgen, *Chem. Mater.* **12**, 2882 (2000).
- ³⁰ E. Ruff, S. Widmann, P. Lunkenheimer, V. Tsurkan, S. Bordács, I. Kézsmárki, and A. Loidl, *Sci. Adv.* **1**, e1500916 (2015).
- ³¹ Z. Wang, E. Ruff, M. Schmidt, V. Tsurkan, I. Kézsmárki, P. Lunkenheimer, and A. Loidl, *Phys. Rev. Lett.* **115**, 207601 (2015).
- ³² D. Ehlers, I. Stasinopoulos, V. Tsurkan, H.-A. Krug von Nidda, T. Fehér, A. Leonov, I. Kézsmárki, D. Grundler, and A. Loidl, *Phys. Rev. B* **94**, 014406 (2016).
- ³³ A. O. Leonov and I. Kézsmárki, *Phys. Rev. B* **96**, 214413 (2017).
- ³⁴ A. Mehlin, F. Xue, D. Liang, H. F. Du, M. J. Stolt, S. Jin, M. L. Tian, and M. Poggio, *Nano Lett.* **15**, 4839 (2015).
- ³⁵ B. Gross, D. P. Weber, D. Ruffer, A. Buchter, F. Heimbach, A. Fontcuberta i Morral, D. Grundler, and M. Poggio, *Phys. Rev. B* **93**, 064409 (2016).
- ³⁶ A. Mehlin, B. Gross, M. Wyss, T. Schefer, G. Tütüncüoğlu, F. Heimbach, A. Fontcuberta i Morral, D. Grundler, and M. Poggio, *Phys. Rev. B* **97**, 134422 (2018).
- ³⁷ K. A. Modic, M. D. Bachmann, B. J. Ramshaw, F. Arnold, K. R. Shirer, A. Estry, J. B. Betts, N. J. Ghimire, E. D. Bauer, M. Schmidt, M. Baenitz, E. Svanidze, R. D. McDonald, A. Shekhter, and P. J. W. Moll, *Nat. Commun.* **9**, 3975 (2018).
- ³⁸ D. Rugar, H. J. Mamin, and P. Guethner, *Appl. Phys. Lett.* **55**, 2588 (1989).
- ³⁹ E. Neuber, P. Milde, A. Butykai, S. Bordács, H. Naka-

mura, T. Waki, Y. Tabata, K. Geirhos, P. Lunkenheimer,

I. Kézsmárki, P. Ondrejovic, J. Hlinka, and L. M. Eng,
J. Phys. Condens. Mater. **30**, 445402 (2018).